

A millimeter methanol maser ring tracing the deceleration of the heat wave powered by the massive protostellar accretion outburst in G358.93–0.03 MM1

T. R. HUNTER,¹ C. L. BROGAN,^{1,2} G. C. MACLEOD,^{3,4} C. J. CYGANOWSKI,⁵ R. A. BURNS,^{6,7} AND B. A. MCGUIRE^{8,1}

¹*National Radio Astronomy Observatory, 520 Edgemont Rd, Charlottesville, VA 22903, USA*

²*Department of Astronomy, University of Virginia, P.O. Box 3818, Charlottesville, VA 22904, USA*

³*Xinjiang Astronomical Observatory, Chinese Academy of Sciences, Urumqi 830011, People's Republic of China*

⁴*Hartebeesthoek Radio Astronomy Observatory, PO Box 443, Krugersdorp 1740, South Africa*

⁵*SUPA, School of Physics and Astronomy, University of St. Andrews, North Haugh, St. Andrews KY16 9SS, UK*

⁶*RIKEN Pioneering Research Institute, 2-1 Hirosawa, Wako-shi, Saitama, 351-0198, Japan*

⁷*Engineering Research Institute “Ventspils International Radio Astronomy Centre”, Ventspils University of Applied Sciences, Inženieru iela. 101, Ventspils, LV-3601, Latvia*

⁸*Department of Chemistry, Massachusetts Institute of Technology, Cambridge, MA 02139, USA*

(Received Nov 14, 2025; Revised Dec 26, 2025; Accepted Dec 30, 2025)

ABSTRACT

We present multi-epoch, multi-band ALMA imaging of the new Class II millimeter methanol masers excited during the accretion outburst of the massive protostar G358.93–0.03 MM1. The highest angular resolution image (24 mas \approx 160 au) reveals a nearly complete, circular ring of strong maser spots in the 217.2992 GHz ($v_t=1$) maser line that closely circumscribes the dust continuum emission from MM1. Weaker maser emission lies inside the eastern and southern halves of the maser ring, generally coincident with the centimeter masers excited during the outburst, but avoiding the densest parts of the hot core gas traced by high excitation lines of CH₃CN. Using a variety of fitting techniques on the image cubes of the two strongest maser lines, each observed over 3–4 epochs, we find the diameter of the ring increased by \gtrsim 60% (from \approx 1100 to \approx 1800 au in the 217 GHz line) over 200 days, consistent with an average radial propagation rate of \approx 0.01c, while the maser intensity declined exponentially. Fitting the angular extent of the millimeter masers versus time yields a power law of index 0.39 ± 0.06 , which also reproduces the observed extent of the 6.7 GHz masers in the first VLBI epoch of R. A. Burns et al. (2020). This exponent is consistent with the prediction of radius vs. time in the Taylor-von Neumann-Sedov self-similar solution for an intense spherical explosion from a point source ($R \propto t^{2/5}$). These results demonstrate the explosive nature of accretion outbursts in massive protostars and their ability to generate subluminal heat waves traceable by centimeter and millimeter masers for several months as the energy traverses the surrounding molecular material.

Keywords: accretion, accretion disks — ISM: molecules — ISM: individual objects (G358.93-0.03) — masers — stars: formation — stars: protostars

1. INTRODUCTION

The discoveries of powerful accretion outbursts in two high-mass protostars – NGC6334I-MM1 (T. R. Hunter et al. 2017, 2021) and S255IR-NIRS3 (A. Caratti o Garatti et al. 2017; S.-Y. Liu et al. 2018) – provided crucial insights on the role of episodic accretion in massive star formation (C. L. Brogan et al. 2018; R. Ce-

saroni et al. 2018). While a study of Orion suggests that episodic accretion accounts for \gtrsim 25% of a star's mass (W. J. Fischer et al. 2019), hydrodynamic simulations of massive protostars predict values up to 40–60% (D. M.-A. Meyer et al. 2021), making it a key phenomenon to understand the process of massive star formation. Both aforementioned outbursts were heralded by Class II 6.7 GHz CH₃OH maser flares in single dish observations (G. C. MacLeod et al. 2018; M. Szymczak et al. 2018; K. Fujisawa et al. 2015), and subsequent high resolution studies confirmed that the maser flares

occurred in dense gas surrounding the outbursting protostar (T. R. Hunter et al. 2018; L. Moscadelli et al. 2017). Because Class II CH₃OH masers are pumped by infrared radiation (D. M. Cragg et al. 2005), their apparent association with protostellar luminosity outbursts has a theoretical basis. Thus, identifying and characterizing more events is critical to understanding massive star formation.

On 2019 January 14, the 6.7 GHz Class II CH₃OH maser line in the massive star-forming region G358.93–0.03 began flaring, rising in flux by an order of magnitude from 10 Jy (J. L. Caswell et al. 2010) to 99 Jy in two weeks (K. Sugiyama et al. 2019), and ultimately reaching 1156 Jy after seven weeks (G. C. MacLeod et al. 2019). With no prior (sub)millimeter interferometric observations, this region was known primarily as a compact clump in single dish (sub)millimeter continuum surveys, including the 1.1 mm BOLOCAM Galactic Plane Survey (BGPS) (G358.936-00.032, E. Rosolowsky et al. 2010) and the 0.87 mm ATLASGAL survey (AGAL358.931-00.029, J. S. Urquhart et al. 2013), with a near kinematic distance of 6.75 kpc (C. L. Brogan et al. 2019).

Because the strength and rapid rise of the 6.7 GHz CH₃OH maser flare in G358.93–0.03 indicated a potential accretion outburst event, the Maser Monitoring Organization (M2O)⁹ pursued multi-wavelength follow-up with telescopes worldwide. This effort led to the unprecedented discovery of several never-before-seen Class II CH₃OH maser lines, including some in torsionally-excited ($v_t \geq 1$) states (S. L. Breen et al. 2019; A. E. Volvach et al. 2020; G. C. MacLeod et al. 2019; D. Miao et al. 2022; B. R. Johnson et al. 2025). In March and April 2019, 14 new CH₃OH maser lines (11 from $v_t=1$ and one from $v_t=2$) were detected by the Submillimeter Array (SMA) and the Atacama Large Millimeter/submillimeter Array (ALMA). All the new masers showed a curvilinear spatial velocity pattern closely surrounding the dominant (sub)millimeter continuum source (MM1) in a protocluster comprised of (at least) 8 members. VLBI observations of the well-known 6.7 GHz maser line ($v_t=0$) spanning the month of February led to the discovery of a heat wave propagating outward from a location consistent with MM1, adding weight to the hypothesis of a protostellar outburst in MM1 (R. A. Burns et al. 2020).

Subsequent analysis of multi-epoch archival mid- to far-infrared data combined with new observations with SOFIA found a luminosity increase of a factor of $4.7^{+2.1}_{-1.5}$, confirming an accretion outburst in MM1 (B. Steck-

lum et al. 2021). Of the handful of known events, the G358.93–0.03 MM1 accretion outburst has the shortest duration (see Table 3 of V. G. Elbakyan et al. 2024). In addition, light curves of the more common cm-wavelength CH₃OH maser lines ($v_t=0$) from Hartbeesthoek Radio Observatory (G. C. MacLeod et al. 2019) show that the G358.93–0.03 masers reached their peak in 7–10 weeks, much more rapidly than in NGC6334I-MM1 (8 months, G. C. MacLeod et al. 2018) and S255IR-NIRS3 (5 months, M. Szymczak et al. 2018). In light of the results from hydrodynamic simulations of accretion in massive protostars, which predict multiple outbursts with a range of magnitudes during the protostellar stage (D. M.-A. Meyer et al. 2019a,b), it is critical to learn as much as possible from each observed event. The multi-epoch cm-wavelength VLBI campaign of R. A. Burns et al. (2023) revealed expanding rings of methanol masers which, when combined into a single map, provided a sparsely sampled view of the gas kinematics within a rotating accretion disk with a spatial resolution sufficient to reveal spiral arms in the disk. These data also traced the propagation speed of the heat-wave at early times. In this paper, we show for the first time that the SMA and ALMA can be used to trace rings of mm-wavelength CH₃OH maser emission which are also driven by the heat-wave. The size of the mm maser rings evolves with time, allowing us to measure the deceleration of the heat wave over 200 days.

2. OBSERVATIONS

The observing parameters of our new ALMA data are summarized in Table 1. The ALMA data were calibrated using the ALMA pipeline (T. R. Hunter et al. 2023) packaged with CASA (CASA Team et al. 2022). In all cases, the target was observed at the phase center, and interactive self-calibration was performed on the strongest maser line with solutions transferred to all spectral windows with linear phase delay correction. Particularly for the longest baseline epoch (2019.451), this technique enabled unusually high-fidelity in the 25 mas resolution 1.3 mm continuum image. The SMA observations and data reduction are described in C. L. Brogan et al. (2019). For this paper, higher angular resolution SMA maser cubes were constructed using superuniform (SU) weighting (D. S. Briggs et al. 1999). The properties of all the image cubes are summarized in Table 1. The transition information for the two maser lines studied and those to which they are compared in this paper is given in Table 2.

⁹ See the M2O website at MaserMonitoring.org

Table 1. Properties of the observations and the spectral line cubes

Array	Rest Freq. ^a (GHz)	Epoch (#: year)	Weight (robust)	Beamsize ("×" (P.A. in deg))	Peak intensity (Jy beam ⁻¹)	Peak velo. (km s ⁻¹)	RMS noise: (mJy beam ⁻¹)	Min–Max ^d (K)	
Details of CH ₃ OH maser line cubes									
SMA vex	199.5749	1: 2019.196	SU	0.619×0.403 (+12)	1203	149000	−15.52	110–900	14–110
ALMA C4	199.5749	2: 2019.286	SU	0.366×311 (−25)	252	68300	−15.28	4.7–34	1.3–9.1
ALMA C8	199.5749	3: 2019.552	0	0.064×0.041 (+23) ^b	1.1	12400	−16.60	8.2–17	12.2–4.5
SMA vex	217.2992	1: 2019.196	SU	0.587×0.370 (+11)	157	18700	−15.52	85–173	10–21
ALMA C10	217.2992	2: 2019.451	0.5	0.025×0.021 (−65) ^c	9.0	450000	−15.88	11–251	1.3–30
ALMA C8	217.2992	3: 2019.538	0.5	0.087×0.059 (−25) ^c	8.8	44500	−15.76	7.5–19	0.9–2.3
ALMA C6	217.2992	4: 2019.747	−1	0.177×0.124 (−86) ^c	4.8	5700	−15.76	8.7–19	1.0–2.3
Details of thermal (non-maser) line cubes									
ALMA C8	199.5749	5: 2021.599	0.4	0.076×0.059 (+65)	0.022	152	−17.68	2.5–2.9	17–20
ALMA C8	217.2992	5: 2021.597	0.5	0.063×0.052 (+81)	0.018	146	−16.96	1.3–1.7	10–13
ALMA C8	202.1648	5: 2021.597	0.4	0.070×0.050 (+66)	0.016	120	−17.68	2.3–2.4	17–18
ALMA C8	220.6793	5: 2021.597	0.5	0.063×0.052 (+80)	0.015	115	−17.32	1.7–1.9	13–15
ALMA C8	220.5393	5: 2021.597	0.5	0.063×0.052 (+80)	0.016	121	−17.68	1.6–1.8	12–14

^aFinal three rows are CH₃CN: $J=11–10$ $K=7$, $J=12–11$ $K=4$, and $J=12–11$ $K=7$, respectively.

^bPrior to the 2-component fitting process, this cube was smoothed to the beamsize of the 2019.286 epoch (see § 3.4).

^cSame as ^b but smoothed to the beamsize of the SMA epoch (see § 3.4).

^dRange of RMS per channel where channel width = 0.12 km s⁻¹ (ALMA CH₃OH), 0.24 km s⁻¹ (SMA), and 0.36 km s⁻¹ (CH₃CN).

Table 2. Properties of the CH₃OH maser transitions

Frequency ^a (GHz)	Symmetry & Transition $\sigma, J(K) - J'(K'), v_t$	E_{up}/k	Ref. ^b (K)
observed lines			
199.574851(18)	$E_2, 13(-2) - 14(-3), v_t=1$	575.18	1
217.299205(17)	$A^-, 6(1) - 7(2), v_t=1$	373.92	1
compared lines			
6.6685192(8)	$A^+, 5(1) - 6(0), v_t=0$	49.06	2
20.970620(21)	$A^+, 10(1) - 11(2), v_t=1$	452.44	1

^aUncertainty in final digit(s) given in parentheses.

^bReferences: (1) CDMS (C. P. Endres et al. 2016), (2) (H. S. P. Müller et al. 2004)

3. RESULTS

3.1. Maser morphology at highest resolution

The sequence of ALMA observations were obtained over many months as the antennas were moved to larger then smaller configurations. The highest angular resolution image of the millimeter masers in G358.93–0.03 (160 au) was obtained in epoch 2019.451, in the 217.2992 GHz *A*-type CH₃OH line. The peak intensity (moment 8) image reveals a striking ring-like structure that circumscribes the dust continuum emission, which has an extent of 0''.24 ∼1600 au (Fig. 1a, 2b). The ring is nearly complete except on the northern edge, where the gap contains a secondary peak of continuum emission. Two cm maser lines of *A*-type CH₃OH were observed within a few days of this image, 6.668 GHz ($v_t=0$) with VLBI (R. A. Burns et al. 2023) and 20.97062 GHz ($v_t=1$) with the Karl G. Jansky Very Large Array (O. S. Bayandina et al. 2022), and those spots all lie inside the ring of strongest 217 GHz maser emission. Extended 217 GHz maser emission is present inside the ring (Fig. 1a) with a brightness tem-

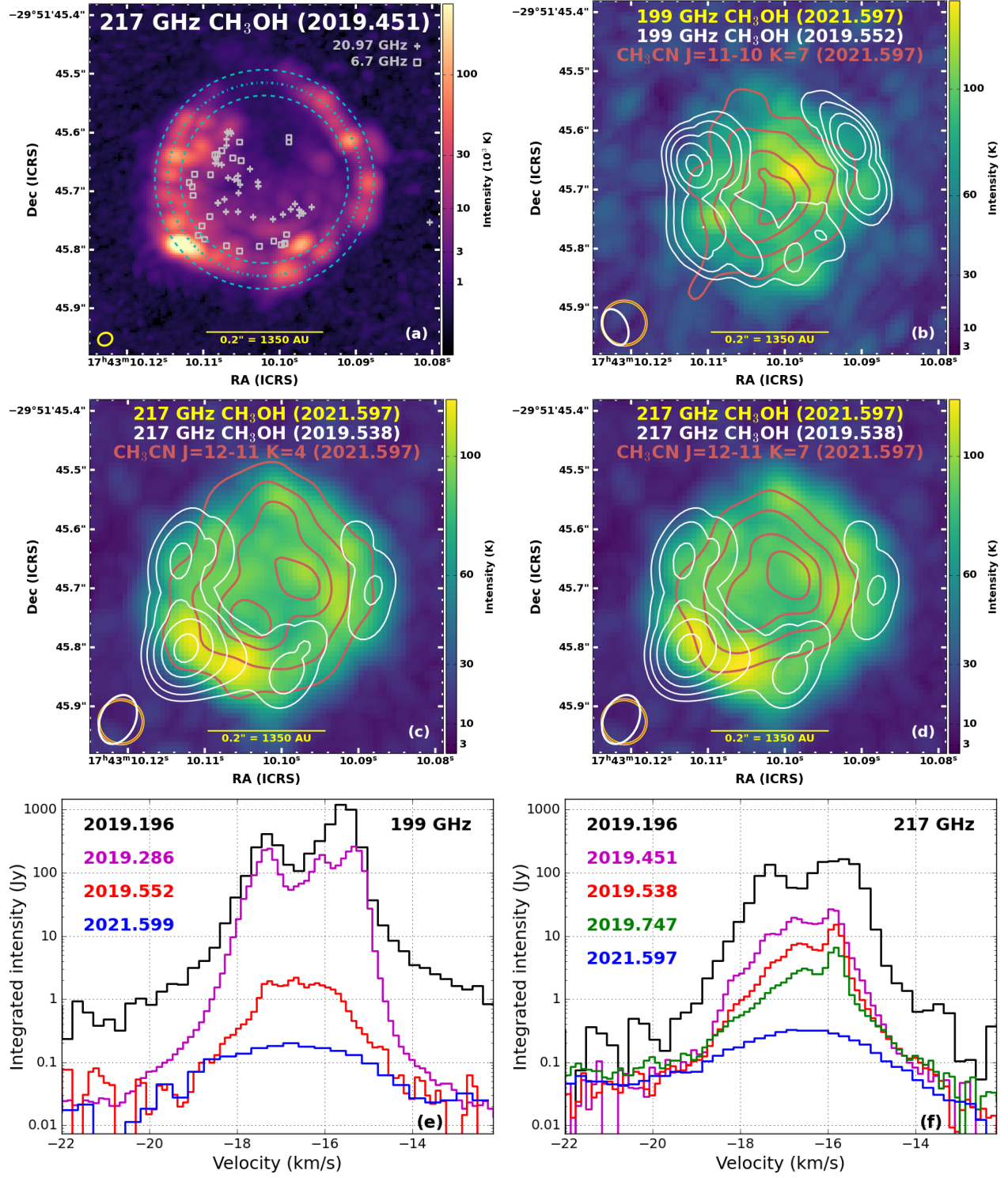


Figure 1. (a) Peak intensity image of the 217 GHz masers surrounding MM1 at Epoch 2019.451 with squares marking 6.7 GHz maser spots at Epoch 2019.429 from R. A. Burns et al. (2023) and + signs marking 20.9706 GHz maser spots at Epoch 2019.421 from O. S. Bayandina et al. (2022). The blue dash-dotted circle is a fit to the Gaussian-fitted positions of the 8 strongest spatial components around the ring, while the dashed circles represent the 1 σ uncertainty on the fit. Panels (b-d) show in colorscale the peak intensity of the 199 GHz (b) and 217 GHz (c, d) CH₃OH transitions, smoothed to 0. $075''$ resolution, from the 2021.6 epoch data when the emission is consistent with thermal excitation. White contours show the peak intensity of the 199 GHz (b) and 217 GHz (c, d) CH₃OH lines while they were still strongly masering circa 2019.5 (levels: 5, 10, 20, 40, 80% of the maser peak). Also overlaid on (b-d) are red contours of the CH₃CN integrated intensity, smoothed to 0. $075''$ resolution, for the J=11-10 K=7, J=12-11 K=4, and J=12-11 K=7 transitions, respectively (levels: 25, 50, 75, 90% of the peak). Panels (e-f) show spectra of the central 10 km s $^{-1}$ spatially integrated over the region of significant emission at each of the epochs from Table 1.

perature still well above the upper level excitation energy of this transition ($E_{\text{up}}=374$ K). In many channels, 217 GHz maser emission appears on both sides of the ring, which will produce blending in lower resolution images. In hindsight, fitting a single spatial component to such images (as in C. L. Brogan et al. 2019) will lead to biased estimates of the emission extent. Therefore, the extent of the fitted pattern of masers in the low resolution epochs must be revisited (see § 3.3).

3.2. Exponential decay into thermal emission

The strongest CH₃OH maser lines observed in ≥ 3 epochs were the 199 and 217 GHz lines, thus we use their data in our analysis. In both cases, the first epoch is from SMA, which had the coarsest angular resolution, while the rest are from ALMA (Table 1). The first epoch corresponds to 14 days after the second 6.7 GHz epoch of R. A. Burns et al. (2020), whereupon the 6.7 GHz maser extent had reached a diameter of ~ 1000 au (R. A. Burns et al. 2020). It is also only 2 days after the 12.178 and 6.7 GHz masers had reached their peak single-dish intensities (G. C. MacLeod et al. 2019). Both millimeter maser lines (199 and 217 GHz) decayed exponentially (Fig. 3a), with fitted e-folding times of 19.7 ± 0.38 and 61.7 ± 7.4 days, respectively, for their peak intensities, and 20.0 ± 0.5 and 44.9 ± 8.5 days for their integrated flux densities. The 217 GHz line shows a significantly slower rate of decline, making it detectable for the longest duration among the five millimeter methanol maser lines observed by SMA or ALMA for at least 3 epochs during 2019¹⁰. Exponential decay of CH₃OH maser emission was also observed during the S255IR-NIRS3 outburst (6.7 GHz, M. Szymczak et al. 2018) and in single-dish observations of G358.93–0.03: six lines in the 3 mm band (S.-j. Zhang et al. 2024) and two lines of ¹³CH₃OH in Ku band (X. Chen et al. 2020).

By the time of our ALMA observations on 2021.597, the 199 and 217 GHz lines were considerably weakened, with peak intensities similar to the other bright thermal hot core lines in MM1 (Table 1). Their brightness temperatures were significantly below the excitation energy levels of these transitions (Table 2), and their line profiles were Gaussian shaped in the central 5 km s^{-1} instead of the prior multi-peaked profile (Figure 1e,f). These two attributes indicate that these transitions were no longer masering. The morphology of the residual thermal CH₃OH emission (Fig. 1b,c,d) spans essentially the same diameter as the maser emission observed two years

prior, though the spatial peaks generally do not coincide. Other hot core species tracing dense gas with a similar E_{up} as the 217 GHz line, such as CH₃CN $K=7$ from $J=11\text{--}10$ and $J=12\text{--}11$ (Fig. 2b,d), arise mostly inside the (former) maser ring. The strongest emission of the higher-lying 199 GHz thermal line ($E_{\text{up}}=575$ K) originates from close to the $K=7$ peaks ($E_{\text{up}}=408\text{--}419$ K). While the extents of these CH₃CN lines are comparable to thermal CH₃OH, their peak intensities are not correlated with the coeval thermal or (prior) masering CH₃OH gas.

3.3. Maser position fitting technique

Image cubes from three ALMA epochs have sufficient angular resolution to independently fit several maser spots around the ring. To measure the ring diameter, we subsequently fit those positions with a circle using `scipy.odr` accounting for the uncertainties of those fitted positions, with results summarized in Table 3 and Fig. 2b,c. The offsets of the centers of the fitted circles from the continuum peak range from 7–16 mas (50–110 au). In the other four epochs, although the ring is not clearly resolved, the emission is extended east–west. Fortunately, even the lowest angular resolution SMA cubes from the first epoch, when the maser lines were strongest, allow two spatial components to be fit reliably in channels with sufficiently high S/N and thereby provide a potential method to measure changes in the structure.

To establish the effectiveness of 2-component fitting of this structure, we performed a proof-of-concept test by smoothing the highest resolution ALMA cube of the 217.2992 GHz line (i.e., the second epoch: 2019.451) to the much lower resolution of the SMA epoch (Table 1). First, we examined the native resolution ALMA cube and marked two spots in each channel: the brightest spot in each of the eastern and western halves of the ring. We ran the CASA task `imfit` to fit two Gaussians to each channel of the smoothed cube using these initial position estimates. We fixed the size and position angle of each component to the synthesized beamsize and solved for their positions and intensities. In the channels where the fitting task succeeded mathematically, we examined the locations of the fitted components and the residual images and established several criteria to determine if a 2-component fit was robust and reliable. First, the peak absolute intensity in the residual image of the 2-component fit must be < 0.4 times that of a single-component fit to the same channel. Second, the integrated absolute flux in the residual image of the 2-component fit must be < 0.6 that of a single-component fit. These two requirements demon-

¹⁰ The other three lines are the 200, 201, and 215 GHz $v_t=1$ lines; see Table 3 of C. L. Brogan et al. (2019) for their frequencies and E_{up} values.

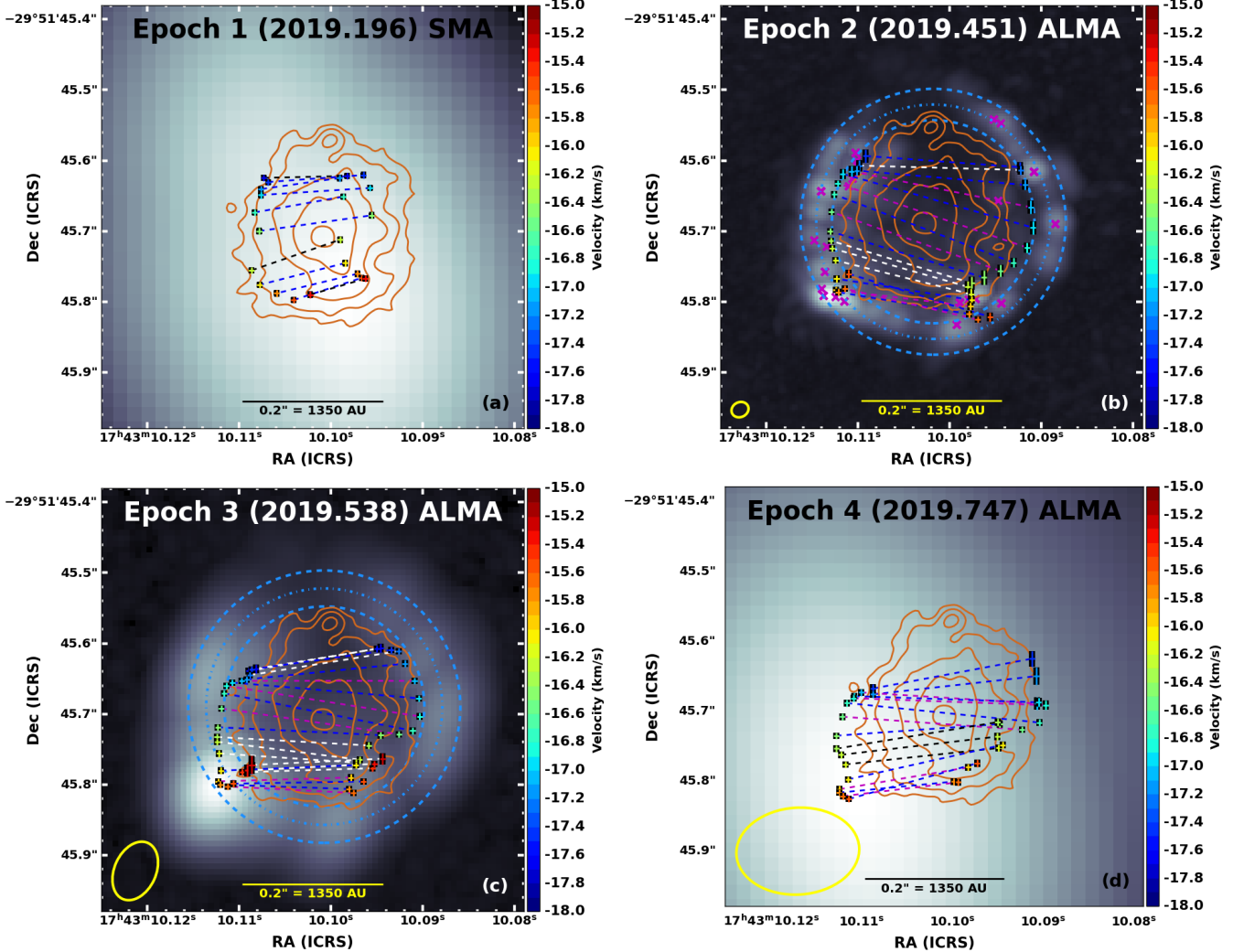


Figure 2. Native resolution peak intensity images of the 217 GHz maser emission in greyscale, ordered by epoch, overlaid with 217 GHz continuum contours from epoch 2019.538 ($0.05, 0.1, 0.2, 0.4, 0.8 \text{ Jy beam}^{-1}$), and marked with the 2-component fits as crosses colored by velocity and connected to their counterparts by dashed lines. The initial estimates are shown as magenta X's in panel b. Blue dashed lines denote channels fit successfully across all epochs, magenta dashed lines denote channels fit successfully across only the ALMA epochs, while white and black dashed lines denote the remaining channels fit successfully in two or fewer epochs. The blue circles in panels b and c are the circle fits (§ 3.3) for their epochs, with the dashdot circle being the best fit and the dashed circles representing the 1σ uncertainties.

strate that a 2-component fit is significantly more effective in modeling the total flux. Third, the separation of the fitted components in right ascension must be between $0.^{\circ}09$ and $0.^{\circ}40$. The lower limit avoids solutions where the two components are nearly coincident (i.e. on the same side of the ring) and the upper limit avoids anomalous fits far outside the ring. To check the fit robustness, 2-component fits were also run with the initial estimates set to two locations separated by $0.^{\circ}18$ straddling the single component fit; we confirmed that nearly identical fit results were still obtained. To check the fit reliability, we overlaid the reliable 2-component fit results on the peak intensity image of the native-resolution

parent data, demonstrating that the fitted positions generally follow the true underlying structure in the two highest resolution ALMA epochs (Fig. 2b,c) to within the native beamsize. However, the 2-component fit results systematically tend to agree with the -1σ diameter from the ring fit rather than the fitted diameter, hence the results from these two distinct methods should not be combined when fitting for the time variation.

Assuming the ring-like structure was pervasive in time, we performed the same spatial smoothing to the SMA cube resolution for the other ALMA epochs at 217.2992 GHz, followed by 2-component fitting using the same initial estimates as epoch 2019.451 with the same

process and success criteria. This method ensures a globally self-consistent fitting approach across epochs and observatories while not imposing any assumption of a smaller diameter at earlier epochs. The same method was applied to the 199.5749 GHz line, but the maser was too weak in the final ALMA epoch to achieve 2-component fits after smoothing it to the SMA resolution. Therefore, we smoothed the final ALMA epoch cube to the lower resolution ALMA epoch and fit that cube with the same process. Finally, we fit the SMA cubes for both lines with this process, applying the astrometric shifts required (C. L. Brogan et al. 2019).

3.4. Maser fitting results

The successful 2-component fit results from both observatories for the 217 GHz line are illustrated in Figure 2. The lengths of the lines connecting the two components in each channel reveal a trend of increasing separation with time. Within each epoch, a range of separations is found, in part due to the velocity structure of the ring where different chord lengths are traced in different channels as the emission moves along the ring (mostly in declination). Since the diameter is the largest chord of a circle, we take the 90th percentile measurement as the best estimate of the diameter, with the estimated uncertainty being the difference between it and the 80th and 100th percentile values. To reflect the additional uncertainty of fitting relative separations smaller than the observed beamsize (θ), we add in quadrature the ratio of θ to the median SNR of the individual separation measurements.

The fit results for each epoch of each line are listed in Table 3 and illustrated in Figure 3b. The results indicate a general trend that the emission diameter increased with time. Also shown in Fig. 3b are measurements of the diameter of the distribution of 6.7 GHz maser spots fit to 5 epochs of VLBI images by R. A. Burns et al. (2023). Here, the diameter is taken as the smallest circle containing 90% of the fitted spots and the uncertainties correspond to the smallest circles containing 80% and 100% of the spots. Fitting the inferred diameters from the 2-component fits to the millimeter maser images using a fractional power law, $R = a(t - t_0)^m$, assuming $R=0$ at $t=t_0=2019.0479$ corresponding to the maser flare inception (K. Sugiyama et al. 2019) yields $m = 0.39 \pm 0.06$. The width of the 90% confidence region of the fit shown in Fig. 3b corresponds to the interdecile range of 50000 Monte Carlo trial fits with bootstrap resampling. This fit is consistent with the size measurement of the first epoch of 6.7 GHz masers. However, an independent fit to all five epochs of the 6.7 GHz maser spot extent measurements, including

four epochs obtained amidst the millimeter maser measurements, produces a shallower power law index. These results demonstrate that one should be cautious and not simply combine size measurements from maser transitions that likely exhibit population inversion in different ranges of physical conditions, particularly when detailed theoretical models are not available for all transitions. In this case, the 6.7 GHz line commonly observed as a strong maser in many high-mass star formation regions (J. L. Caswell et al. 2010) is known to show population inversion for a wide range of physical conditions (D. M. Cragg et al. 2005). In contrast, the rarer transitions like the 199 and 217 GHz lines likely show significant population inversion for a relatively narrower range of physical conditions, only (to date) observed in accretion bursts.

Table 3. Summary of maser fitting results

Epoch (year)	Frequency (GHz)	No. spots	Inferred diameter (arcsec)	Inferred diameter (AU)
ring fitting of high resolution ALMA cubes				
2019.451	217.2992	8	0.336 ± 0.047	2270 ± 310
2019.538	217.2992	6	0.335 ± 0.051	2265 ± 345
2019.552	199.5748	7	0.289 ± 0.081	1950 ± 550
2-component fitting of SMA and ALMA cubes				
2019.196	199.5749	7	$0.138_{-0.013}^{+0.014}$	930_{-90}^{+100}
2019.196	217.2992	11	$0.155_{-0.032}^{+0.026}$	1050_{-220}^{+180}
2019.286	199.5749	21	$0.180_{-0.014}^{+0.015}$	1210_{-100}^{+100}
2019.451	217.2992	17	$0.276_{-0.017}^{+0.008}$	1860_{-120}^{+50}
2019.538	217.2992	22	$0.264_{-0.022}^{+0.014}$	1780_{-150}^{+100}
2019.552	199.5749	10	$0.244_{-0.013}^{+0.014}$	1650_{-90}^{+100}
2019.747	217.2992	16	$0.270_{-0.012}^{+0.008}$	1820_{-80}^{+60}
ring inferred from extent of VLBI spot data				
2019.086	6.668	140	$0.080_{-0.003}^{+0.030}$	540_{-20}^{+205}
2019.158	6.668	219	$0.187_{-0.013}^{+0.020}$	1260_{-91}^{+133}
2019.193	6.668	192	$0.192_{-0.012}^{+0.021}$	1297_{-81}^{+143}
2019.377	6.668	70	$0.237_{-0.012}^{+0.025}$	1602_{-83}^{+166}
2019.429	6.668	75	$0.235_{-0.005}^{+0.037}$	1584_{-36}^{+252}

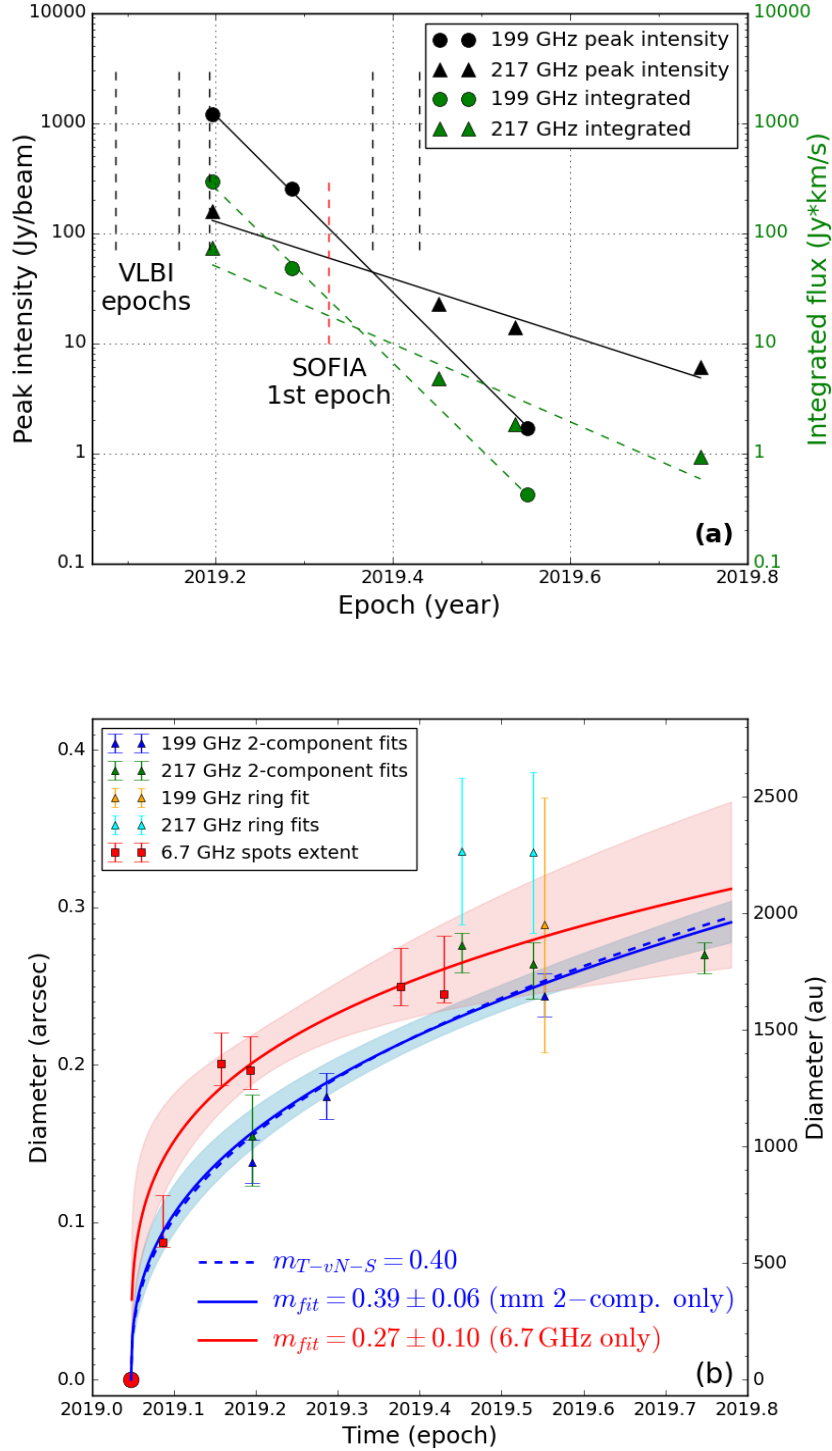


Figure 3. (a) Light curve of the 199 and 217 GHz maser lines on a semi-log scale overlaid by fitted models of exponential decay, with vertical dashed lines denoting the VLBI epochs (R. A. Burns et al. 2020) and first SOFIA epoch (B. Stecklum et al. 2021) for reference; (b) Ring diameter vs. time as inferred from the various maser tracers and methods described in § 3.3. The solid curves are fractional power-law fits to the millimeter maser 2-component fit results from this work (blue) and independently to the 6.7 GHz VLBI measurements (red) from R. A. Burns et al. (2023). The best-fit blue solid curve is consistent with the Taylor-von Neumann-Sedov exponent (blue dashed curve) within the 90% confidence region indicated by the blue shaded area computed from bootstrap analysis (see Section 3.4). The red spot marks the inception of the maser flare (K. Sugiyama et al. 2019). The gap in the red curve near the origin is where the fit would exceed the speed of light.

4. DISCUSSION

4.1. *Propagation of the heat wave*

In the regime of low dust opacity, the heat wave from an accretion outburst propagates outward essentially at the speed of light as thermal energy carried by photons is promptly absorbed by dust grains and re-radiated at longer wavelengths (D. Johnstone et al. 2013). However, at high dust optical depths, the photon mean free path drops and radiative transfer is slowed (V. Wolf 2024). Evidence for this effect around massive protostars was seen first in the outburst of S255IR-NIRS3 where the delay between the rise of pre-existing and new maser components (L. Moscadelli et al. 2017) implied a propagation speed of $\sim 0.15c$ (B. Stecklum et al. 2018). The increase in size of the maser ring around G358.93–0.03 MM1 (Fig. 3b) follows a similar trend to the 6.7 GHz VLBI observations, which show an apparent propagation rate of $\sim 0.08c$ during February 2019 when the diameter increased from ~ 540 au to ~ 1260 au (R. A. Burns et al. 2020). We interpret our new results as tracing the subsequent outward progress of the heat wave over the 14–215 day interval following those February epochs. Based on the millimeter maser data, the extent of the maser emission increased by $\gtrsim 60\%$ (~ 1100 au to ~ 1800 au in the 217 GHz line), corresponding to a mean radial expansion velocity of $0.01c$. The power law fit to the 2-component fits to the millimeter maser cubes is consistent with the prediction of radius vs. time by the Taylor-von Neumann-Sedov self-similar solution for an intense spherical explosion from a point source in a uniform density medium ($R \propto t^{2/5}$, J. L. Taylor 1955; L. I. Sedov 1946). The protostar MM1 is the obvious source of radiative energy as its location, inferred from the peak dust emission, is at the center of the maser ring (Fig. 2b).

The good agreement with a model based on uniform gas density is not unreasonable, because the torsionally-excited millimeter CH_3OH masers, which are tracing the propagation, are likely excited only within a particular range of density and column density. . The dearth of masers toward the peak of the warmest thermal gas tracer (199 GHz, Fig. 1b) likely indicates the density there is high enough to collisionally quench them. Furthermore, the limited extent of thermal emission in epoch 2021.597 (Fig. 1b,c,d) suggests that the maser flare subsidence corresponds to when the heat wave reached a radius where the gas density was too low to sufficiently excite CH_3OH . Regardless, these results provide direct evidence that the heat wave propagated for at least 9 months, decelerating as the explosive na-

ture of the energy released by the accretion outburst traversed the surrounding molecular material.

4.2. *Connection to the infrared continuum decay and the accretion event*

The high line intensities seen during the outburst from G358.93–0.03 MM1 indicate these masers are saturated. In this regime, their intensity scales linearly with the maser optical depth, which in turn scales linearly with the pumping radiation (L. Moscadelli et al. 2017). Class II CH_3OH masers are pumped by mid-infrared radiation (D. M. Cragg et al. 2005), which should lead to a close coupling between the maser intensity and the combined luminosity of the protostar and its accretion disk. Evidence for this coupling has been found in the intermediate mass young stellar object (YSO) G107.298+5.639 (M. Olech et al. 2020). Examples of exponential decay of the infrared continuum have been seen in a variety of outbursting YSOs, from massive (G323.46–0.08, V. Wolf et al. 2024) to low-mass (e.g., T. Wang et al. 2023), and in models of the dust emission from expanding supernova remnants (S. A. Drozdov et al. 2025). In the context of protostellar accretion, magnetohydrodynamic simulations of low-mass protostars with high magnetic fields (2 kG) produce accretion outbursts with exponentially decaying light curves (B. A. L. Gaches et al. 2024). This behavior is due to the magnetic Rayleigh-Taylor fluid instability developing at the radius where the magnetic field truncates the disk leading to magnetospheric accretion (Z. Zhu et al. 2024).

Building on these ideas, one interpretation of the G358.93–0.03 MM1 event is that the mass ultimately accreted (modeled to be $180 M_{\oplus}$, B. Stecklum et al. 2021) entered the existing disk resulting in disk instability and leading to a spike in the accretion rate which initiated the heat wave. The relatively short duration of this outburst argues against bloating of the protostellar photosphere as a significant contributor to the luminosity increase. Because it remains unclear whether the disk or the protostar dominates the total luminosity in massive YSO outbursts, we cannot say whether the subsequent accretion rate remained steady or declined, only that the total luminosity of the disk plus protostar did eventually decay. Similar high resolution observations and analysis of future events, especially with higher cadence monitoring in the infrared and (sub)millimeter, will help to understand the prevalence, behavior, and underlying mechanisms driving these heat waves. Finally, the relatively long exponential decay timescales of the 217 GHz and 93.196 GHz maser lines (61.7 ± 7.4 and 66.6 ± 11.1 days, respectively; this work and S.-j. Zhang et al. (2024)), suggests these lines may offer the most

promise of detection during outbursts in other massive star forming regions. Interestingly, these maser lines lie within 200 MHz of SiO (5–4) and within 25 MHz of N₂H⁺ (1–0), respectively, so there should be a substantial amount of data in the ALMA archive that could be searched for their fleeting appearances in other objects.

ACKNOWLEDGMENTS

The National Radio Astronomy Observatory is a facility of the National Science Foundation operated under agreement by the Associated Universities, Inc. This paper makes use of the following ALMA data: ADS/JAO.ALMA#2018.A.00031.T and 2019.1.00768.S. ALMA is a partnership of ESO (representing its member states), NSF (USA) and NINS (Japan), together with NRC (Canada) and NSC and ASIAA (Taiwan) and KASI (Republic of Korea), in cooperation with the Republic of Chile. The Joint ALMA Observatory is operated by ESO, AUI/NRAO and NAOJ. This research made use of NASA’s Astrophysics Data System, funded by NASA under Cooperative Agreement 80NSSC21M0056. The SMA is a joint project between the Smithsonian Astrophysical Obser-

vatory and the Academia Sinica Institute of Astronomy and Astrophysics and is funded by the Smithsonian Institution and the Academia Sinica. This research used the <https://www.splatalogue.net> spectroscopy database (A. J. Remijan et al. 2007). C.J.C. acknowledges support from the STFC (grant ST/Y002229/1). R.A.B acknowledges support from the Latvian Council of Science project “A single-baseline radio interferometer in a new age of transient astrophysics (IVARS)” (Grant No. lzp-2022/1-0083). The authors wish to recognize and acknowledge the very significant cultural role and reverence that the summit of Maunakea has always had within the indigenous Hawaiian community. We are most fortunate to have the opportunity to conduct observations from this mountain. We thank the anonymous referee for useful suggestions and recommendations that improved the results and analysis in this paper.

Facility: ALMA, SMA

Software: CASA (CASA Team et al. 2022), ALMA pipeline (T. R. Hunter et al. 2023), Astropy (Astropy Collaboration et al. 2013, 2018, 2022), APLpy (T. Robitaille & E. Bressert 2012), NumPy (C. R. Harris et al. 2020), SciPy (P. Virtanen et al. 2020)

REFERENCES

Astropy Collaboration, Robitaille, T. P., Tollerud, E. J., et al. 2013, *A&A*, 558, A33, doi: [10.1051/0004-6361/201322068](https://doi.org/10.1051/0004-6361/201322068)

Astropy Collaboration, Price-Whelan, A. M., Sipőcz, B. M., et al. 2018, *AJ*, 156, 123, doi: [10.3847/1538-3881/aabc4f](https://doi.org/10.3847/1538-3881/aabc4f)

Astropy Collaboration, Price-Whelan, A. M., Lim, P. L., et al. 2022, *ApJ*, 935, 167, doi: [10.3847/1538-4357/ac7c74](https://doi.org/10.3847/1538-4357/ac7c74)

Bayandina, O. S., Brogan, C. L., Burns, R. A., et al. 2022, *A&A*, 664, A44, doi: [10.1051/0004-6361/202244089](https://doi.org/10.1051/0004-6361/202244089)

Breen, S. L., Sobolev, A. M., Kaczmarek, J. F., et al. 2019, *ApJL*, 876, L25, doi: [10.3847/2041-8213/ab191c](https://doi.org/10.3847/2041-8213/ab191c)

Briggs, D. S., Schwab, F. R., & Sramek, R. A. 1999, in Astronomical Society of the Pacific Conference Series, Vol. 180, Synthesis Imaging in Radio Astronomy II, ed. G. B. Taylor, C. L. Carilli, & R. A. Perley, 127

Brogan, C. L., Hunter, T. R., Cyganowski, C. J., et al. 2018, *ApJ*, 866, 87, doi: [10.3847/1538-4357/aae151](https://doi.org/10.3847/1538-4357/aae151)

Brogan, C. L., Hunter, T. R., Towner, A. P. M., et al. 2019, *ApJL*, 881, L39, doi: [10.3847/2041-8213/ab2f8a](https://doi.org/10.3847/2041-8213/ab2f8a)

Burns, R. A., Sugiyama, K., Hirota, T., et al. 2020, *Nature Astronomy*, 4, 506, doi: [10.1038/s41550-019-0989-3](https://doi.org/10.1038/s41550-019-0989-3)

Burns, R. A., Uno, Y., Sakai, N., et al. 2023, *Nature Astronomy*, 7, 557, doi: [10.1038/s41550-023-01899-w](https://doi.org/10.1038/s41550-023-01899-w)

Caratti o Garatti, A., Stecklum, B., Garcia Lopez, R., et al. 2017, *NatPh*, 13, 276, doi: [10.1038/nphys3942](https://doi.org/10.1038/nphys3942)

CASA Team, Bean, B., Bhatnagar, S., et al. 2022, *PASP*, 134, 114501, doi: [10.1088/1538-3873/ac9642](https://doi.org/10.1088/1538-3873/ac9642)

Caswell, J. L., Fuller, G. A., Green, J. A., et al. 2010, *MNRAS*, 404, 1029, doi: [10.1111/j.1365-2966.2010.16339.x](https://doi.org/10.1111/j.1365-2966.2010.16339.x)

Cesaroni, R., Moscadelli, L., Neri, R., et al. 2018, *A&A*, 612, A103, doi: [10.1051/0004-6361/201732238](https://doi.org/10.1051/0004-6361/201732238)

Chen, X., Sobolev, A. M., Breen, S. L., et al. 2020, *ApJL*, 890, L22, doi: [10.3847/2041-8213/ab72a5](https://doi.org/10.3847/2041-8213/ab72a5)

Cragg, D. M., Sobolev, A. M., & Godfrey, P. D. 2005, *MNRAS*, 360, 533, doi: [10.1111/j.1365-2966.2005.09077.x](https://doi.org/10.1111/j.1365-2966.2005.09077.x)

Drozdov, S. A., Dedikov, S. Y., & Vasiliev, E. O. 2025, *Astrophysical Bulletin*, 80, 22, doi: [10.1134/S199034132460090X](https://doi.org/10.1134/S199034132460090X)

Elbakyan, V. G., Nayakshin, S., Caratti o Garatti, A., Kuiper, R., & Guo, Z. 2024, *A&A*, 692, A256, doi: [10.1051/0004-6361/202451758](https://doi.org/10.1051/0004-6361/202451758)

Endres, C. P., Schlemmer, S., Schilke, P., Stutzki, J., & Müller, H. S. P. 2016, *Journal of Molecular Spectroscopy*, 327, 95, doi: [10.1016/j.jms.2016.03.005](https://doi.org/10.1016/j.jms.2016.03.005)

Fischer, W. J., Safron, E., & Megeath, S. T. 2019, *ApJ*, 872, 183, doi: [10.3847/1538-4357/ab01dc](https://doi.org/10.3847/1538-4357/ab01dc)

Fujisawa, K., Yonekura, Y., Sugiyama, K., et al. 2015, *ATel*, 8286

Gaches, B. A. L., Tan, J. C., Rosen, A. L., & Kuiper, R. 2024, *A&A*, 692, A219, doi: [10.1051/0004-6361/202451842](https://doi.org/10.1051/0004-6361/202451842)

Harris, C. R., Millman, K. J., van der Walt, S. J., et al. 2020, *Nature*, 585, 357, doi: [10.1038/s41586-020-2649-2](https://doi.org/10.1038/s41586-020-2649-2)

Hunter, T. R., Brogan, C. L., MacLeod, G., et al. 2017, *ApJL*, 837, L29, doi: [10.3847/2041-8213/aa5d0e](https://doi.org/10.3847/2041-8213/aa5d0e)

Hunter, T. R., Brogan, C. L., MacLeod, G. C., et al. 2018, *ApJ*, 854, 170, doi: [10.3847/1538-4357/aaa962](https://doi.org/10.3847/1538-4357/aaa962)

Hunter, T. R., Brogan, C. L., De Buizer, J. M., et al. 2021, *ApJL*, 912, L17, doi: [10.3847/2041-8213/abf6d9](https://doi.org/10.3847/2041-8213/abf6d9)

Hunter, T. R., Indebetouw, R., Brogan, C. L., et al. 2023, *PASP*, 135, 074501, doi: [10.1088/1538-3873/ace216](https://doi.org/10.1088/1538-3873/ace216)

Johnson, B. R., Ellingsen, S. P., Breen, S. L., et al. 2025, arXiv e-prints, arXiv:2512.01875, doi: [10.48550/arXiv.2512.01875](https://doi.org/10.48550/arXiv.2512.01875)

Johnstone, D., Hendricks, B., Herczeg, G. J., & Bruderer, S. 2013, *ApJ*, 765, 133, doi: [10.1088/0004-637X/765/2/133](https://doi.org/10.1088/0004-637X/765/2/133)

Liu, S.-Y., Su, Y.-N., Zinchenko, I., Wang, K.-S., & Wang, Y. 2018, *ApJL*, 863, L12, doi: [10.3847/2041-8213/aad63a](https://doi.org/10.3847/2041-8213/aad63a)

MacLeod, G. C., Smits, D. P., Goedhart, S., et al. 2018, *MNRAS*, 478, 1077, doi: [10.1093/mnras/sty996](https://doi.org/10.1093/mnras/sty996)

MacLeod, G. C., Sugiyama, K., Hunter, T. R., et al. 2019, *MNRAS*, 489, 3981, doi: [10.1093/mnras/stz2417](https://doi.org/10.1093/mnras/stz2417)

Meyer, D. M.-A., Haemmerlé, L., & Vorobyov, E. I. 2019a, *MNRAS*, 484, 2482, doi: [10.1093/mnras/sty3527](https://doi.org/10.1093/mnras/sty3527)

Meyer, D. M.-A., Vorobyov, E. I., Elbakyan, V. G., et al. 2021, *MNRAS*, 500, 4448, doi: [10.1093/mnras/staa3528](https://doi.org/10.1093/mnras/staa3528)

Meyer, D. M.-A., Vorobyov, E. I., Elbakyan, V. G., et al. 2019b, *MNRAS*, 482, 5459, doi: [10.1093/mnras/sty2980](https://doi.org/10.1093/mnras/sty2980)

Miao, D., Chen, X., Song, S.-M., et al. 2022, *ApJS*, 263, 9, doi: [10.3847/1538-4365/ac9524](https://doi.org/10.3847/1538-4365/ac9524)

Moscadelli, L., Sanna, A., Goddi, C., et al. 2017, *A&A*, 600, L8, doi: [10.1051/0004-6361/201730659](https://doi.org/10.1051/0004-6361/201730659)

Müller, H. S. P., Menten, K. M., & Mäder, H. 2004, *A&A*, 428, 1019, doi: [10.1051/0004-6361:20041384](https://doi.org/10.1051/0004-6361:20041384)

Olech, M., Szymczak, M., Wolak, P., Gérard, E., & Bartkiewicz, A. 2020, *A&A*, 634, A41, doi: [10.1051/0004-6361/201936943](https://doi.org/10.1051/0004-6361/201936943)

Remijan, A. J., Markwick-Kemper, A., & ALMA Working Group on Spectral Line Frequencies. 2007, in *American Astronomical Society Meeting Abstracts*, Vol. 211, 132.11

Robitaille, T., & Bressert, E. 2012, *APLPy: Astronomical Plotting Library in Python*, <http://ascl.net/1208.017>

Rosolowsky, E., Dunham, M. K., Ginsburg, A., et al. 2010, *ApJS*, 188, 123, doi: [10.1088/0067-0049/188/1/123](https://doi.org/10.1088/0067-0049/188/1/123)

Sedov, L. I. 1946, *Journal of Applied Mathematics and Mechanics*, 10, 241

Stecklum, B., Caratti o Garatti, A., Hodapp, K., et al. 2018, in *IAU Symposium*, Vol. 336, *Astrophysical Masers: Unlocking the Mysteries of the Universe*, ed. A. Tarchi, M. J. Reid, & P. Castangia, 37–40, doi: [10.1017/S1743921317010511](https://doi.org/10.1017/S1743921317010511)

Stecklum, B., Wolf, V., Linz, H., et al. 2021, *A&A*, 646, A161, doi: [10.1051/0004-6361/202039645](https://doi.org/10.1051/0004-6361/202039645)

Sugiyama, K., Saito, Y., Yonekura, Y., & Momose, M. 2019, *ATel*, 12446

Szymczak, M., Olech, M., Wolak, P., Gérard, E., & Bartkiewicz, A. 2018, *A&A*, 617, A80, doi: [10.1051/0004-6361/201833443](https://doi.org/10.1051/0004-6361/201833443)

Taylor, J. L. 1955, *The London, Edinburgh, and Dublin Philosophical Magazine and Journal of Science*, 46, 317, doi: [10.1080/14786440308521083](https://doi.org/10.1080/14786440308521083)

Urquhart, J. S., Moore, T. J. T., Schuller, F., et al. 2013, *MNRAS*, 431, 1752, doi: [10.1093/mnras/stt287](https://doi.org/10.1093/mnras/stt287)

Virtanen, P., Gommers, R., Oliphant, T. E., et al. 2020, *Nature Methods*, 17, 261, doi: [10.1038/s41592-019-0686-2](https://doi.org/10.1038/s41592-019-0686-2)

Volvach, A. E., Volvach, L. N., Larionov, M. G., & MacLeod, G. C. 2020, *Astronomy Letters*, 45, 764, doi: [10.1134/S1063773719110082](https://doi.org/10.1134/S1063773719110082)

Wang, T., Li, J., N. Mace, G., et al. 2023, *ApJ*, 957, 8, doi: [10.3847/1538-4357/acf92e](https://doi.org/10.3847/1538-4357/acf92e)

Wolf, V. 2024, arXiv e-prints, arXiv:2405.17048, doi: [10.48550/arXiv.2405.17048](https://doi.org/10.48550/arXiv.2405.17048)

Wolf, V., Stecklum, B., Caratti o Garatti, A., et al. 2024, *A&A*, 688, A8, doi: [10.1051/0004-6361/202449891](https://doi.org/10.1051/0004-6361/202449891)

Zhang, S.-j., Chen, X., Zhang, Y.-K., et al. 2024, *AJ*, 168, 207, doi: [10.3847/1538-3881/ad73bd](https://doi.org/10.3847/1538-3881/ad73bd)

Zhu, Z., Stone, J. M., & Calvet, N. 2024, *MNRAS*, 528, 2883, doi: [10.1093/mnras/stad3712](https://doi.org/10.1093/mnras/stad3712)